International Journal of Geo-Information

MDPI

Supplementary Materials

Integrating Post-Processing Kinematic (PPK)–Structure-from-Motion (SfM) with Unmanned Aerial Vehicle (UAV) Photogrammetry and Digital Field Mapping for Structural Geological Analysis

Daniele Cirillo [1,2,3,*], Francesca Cerritelli [4], Silvano Agostini [5], Simone Bello [2,3], Giusy Lavecchia [2,3] and Francesco Brozzetti [1,2,3]

[1] Laboratorio di Geologia Strutturale Cartografia e Modellazione Geologica, DiSPuTer, Università G. d'Annunzio, Via dei Vestini, 31, 66100 Chieti, Italy;
[2] DiSPuTer, Università G. d'Annunzio, Via dei Vestini, 31, 66100 Chieti, Italy;
[3] CRUST- Centro inteRUniversitario per l'analisi Sismotettonica Tridimensionale, Italy;
[4] Freelance, Viale Amendola 108, 66020 San Giovanni Teatino, Italy;
[5] CAAM, Università G. d'Annunzio, Via dei Vestini, 31, 66100 Chieti, Italy;
* Correspondence: daniele.cirillo@unich.it; Tel.: +39-08713556389

Supplementary Materials:

This supplementary material consists of 13 figures of a Supplementary Text and 2 tables.

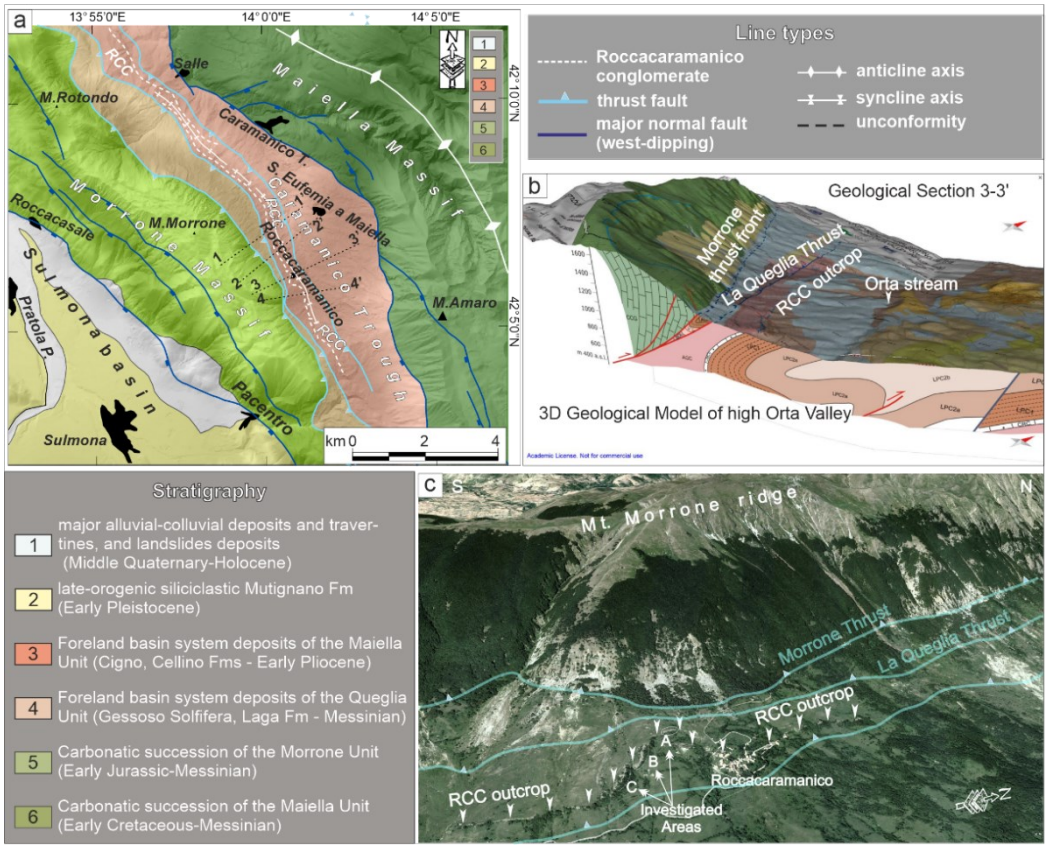

Figure S1. (**a**) Geological Structural Scheme of the near investigated area of Roccacaramanico village; (**b**) Geological cross-section in 3D view (trace 3-3' in the panel a); (**c**) Panoramic view of the study areas (A, B, C) from a satellite image.

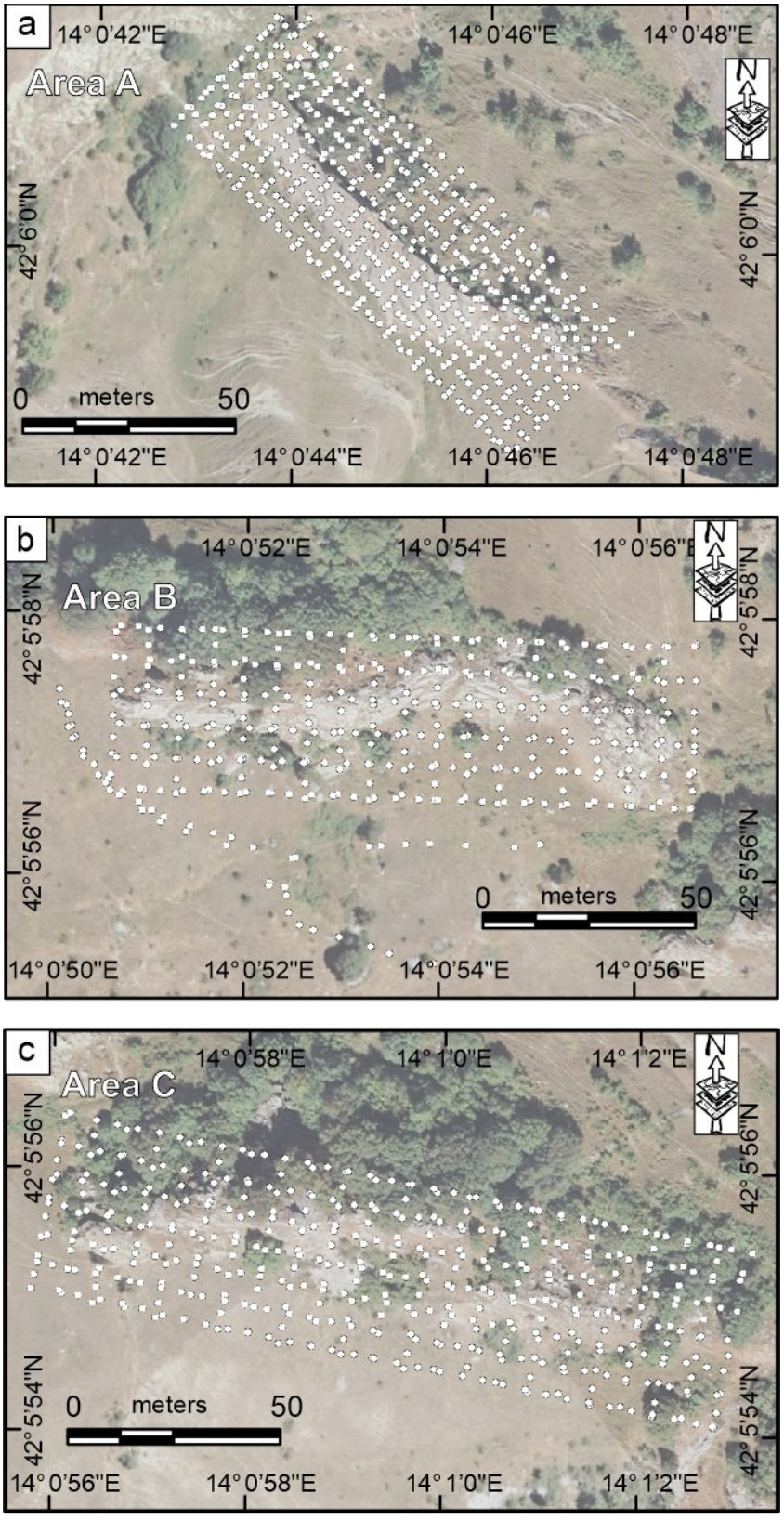

Figure S2. Location of the photographs (small white circles) acquired during the flight missions for area A (**a**), area B (**b**), and area C (**c**)

Supplementary Text 1

PPK Processing – GNSS comparison

In this supplementary material we provide a comparison between the PPK (Post-Processing Kinematic) and GNSS processing method, showing how the PPK has allowed us to reach minimal errors both in the geolocation of the UAV photographs and in the final processing of the Digital Outcrop Models. We provide this example for areas A, B, and C (Figure S3-S6).

The tools used to implement the accuracy of the UAV survey are a GNSS receiver (in our case an Emlid Reach RS2), mounted on a tripod at a height of 2 meters, and a GNSS receiver that records data on a microSD card installed on the UAV. The first works as a Base, while the second works as a Rover. The base receives data both from orbiting satellites (Gps, Glonass, Galileo, Beidou), and from the open-standard correction service of the network of permanent reference stations managed by HxGN SmartNet (https://hxgnsmartnet.com/).

The combined data between the permanent stations and the GNSS used are used to generate corrections in RTK (Real Time Kinematic), via a modem from which a network connection is accessed. This provides reliable, efficient and very accurate positioning (with xyz spatial resolution up to one centimeter).

HxGN SmartNet is the GNSS correction service based on the largest network of reference stations in the world that allows GNSS-enabled devices to quickly determine precise positions.

The post-processing phase is based on the processing of files in RINEX format coming from the rover. The information of the RINEX files allowing to determine the position of the aircraft at any time of the flight. The geolocation data recorded during the flight, allow each single photograph taken in a specified time interval (hh: mm: ss) to record the point in space. The positioning (xyz / Lat, Long, height) is subsequently corrected by using the Toposetter 2.0 software, which allows to change the coordinates in the exif data (EXchangeable Image file Format) contained in the image file of the photograph.

The new coordinates allow the Agisoft Metashape Professional software to better position and manage the point clouds obtained.

We provide herein an estimate of the RMS of our data acquired on the 7 GCPs. The survey of the 7 GCPs carried out using the GNSS Emlid Reach RS2, was done with the RTK correction method in the WGS84 (projection-UTM-zone 33N) coordinate system. The RMS calculated are between 0.01 and 0.015 m for the elevation, while the lateral RMS (xy) varies from 0.0013 and 0.0019 m. As for the standard deviation of the accuracy measured on the GCPs (checkpoints) between the GNSS points and the DOM, the values reach 3 cm and never exceed 7 cm for the entire 3D model.

Throughout the duration of the flights, the base station continuously recorded the position data thanks to the simultaneous presence of a number of satellites between 7 and 15 (Figure S7-S8). The GNSS with the triangulation between the satellites and the fixed stations of the HxGn SmartNet network has received a constant correction thanks also to the internet connection which allowed to connect to the server to reach the nearest permanent base station. For the positioning of the photos, the analysis in PPK made it possible to achieve accuracies well below one centimeter, both in terms of positioning in the elevation and in xy positioning (see Figure S9-S12).

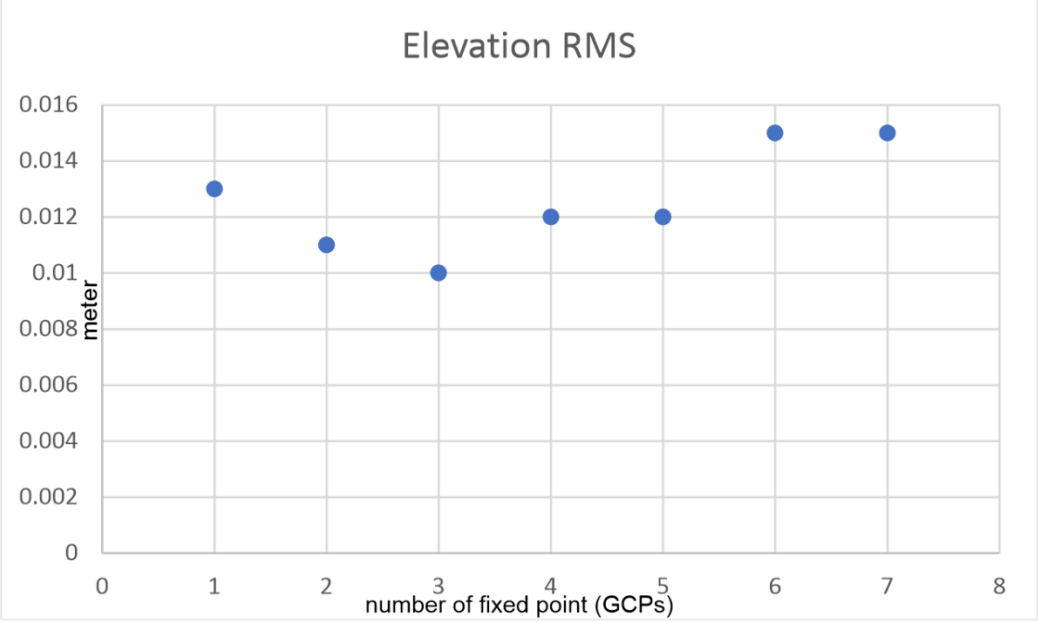

Figure S3. RMS Error (m) in elevation of the seven surveyed GCPs in areas A, B, and C.

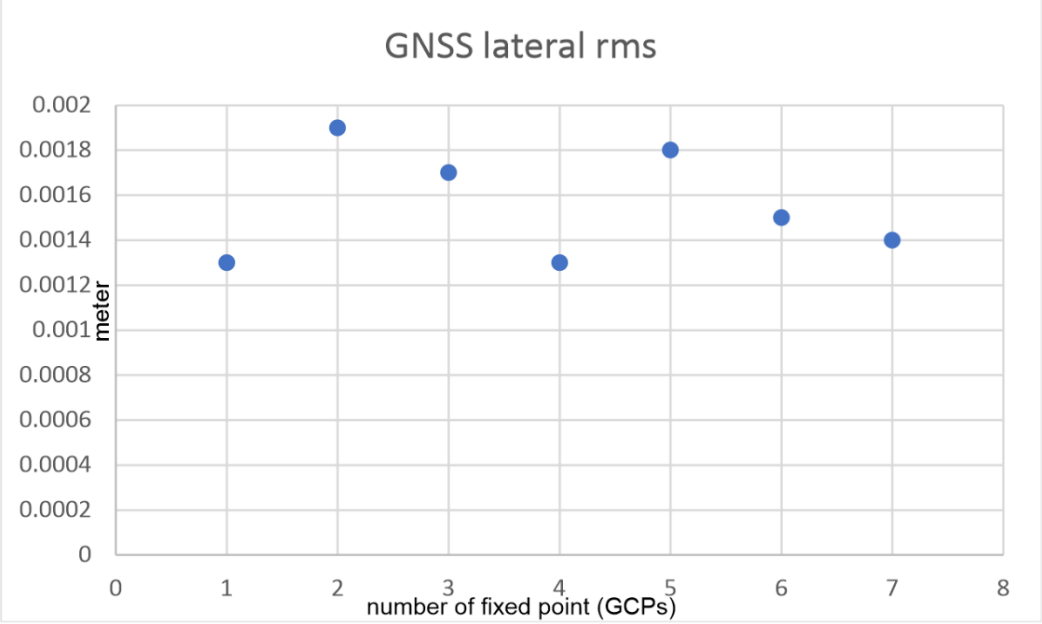

Figure S4. Lateral RMS error (xy) of the seven surveyed GCPs in areas A, B, and C.

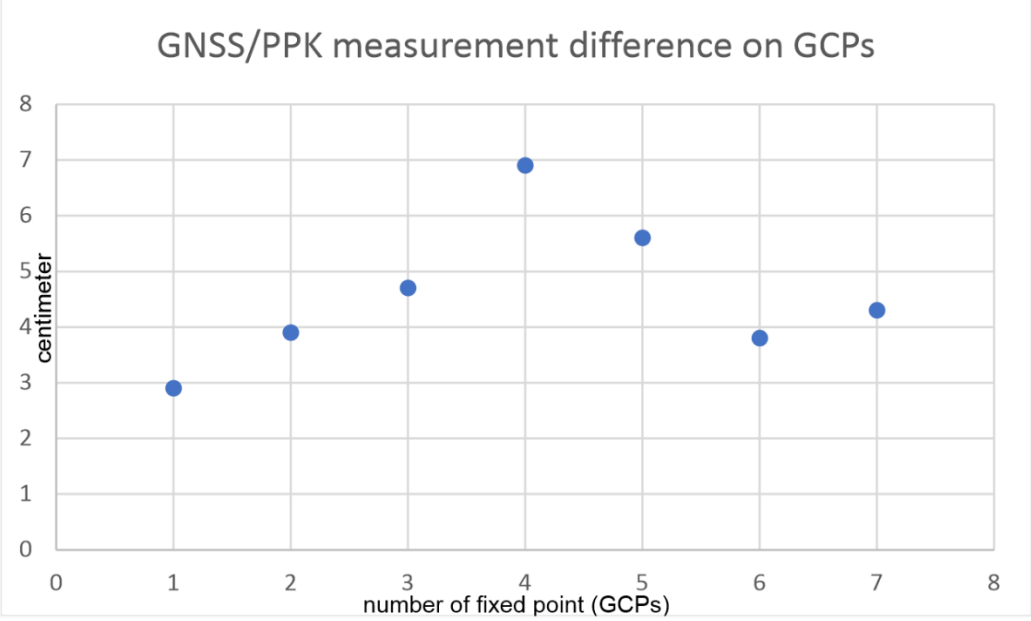

Figure S5. Accuracy of the seven GCPs in areas A, B, and C, surveyed with GNSS Emlid Reach RS2 and DOMs realized.

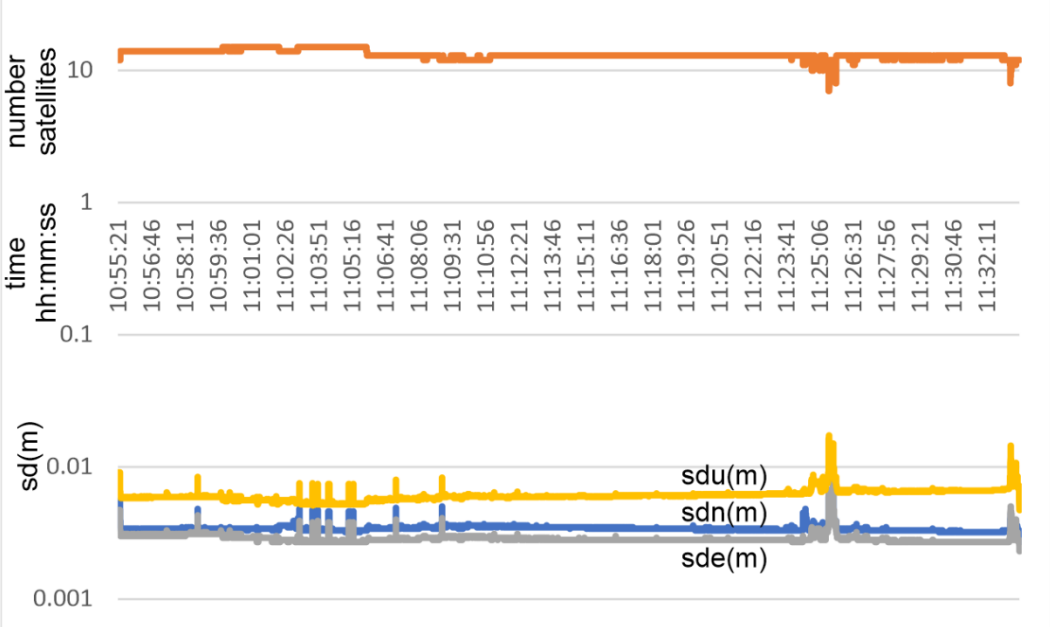

Figure S6. Logarithmic scale at base 10 of the Satellites orbiting during the acquisition of GNSS data (time in UTC at the center of the diagram) and RMS error in XYZ. Orange line: Minimum and a maximum number of satellites received during the GNSS survey; Grey line: Standard Deviation RMS in Easting; Blue line: Standard Deviation RMS in Northening; Yellow line: Standard Deviation RMS in Height.

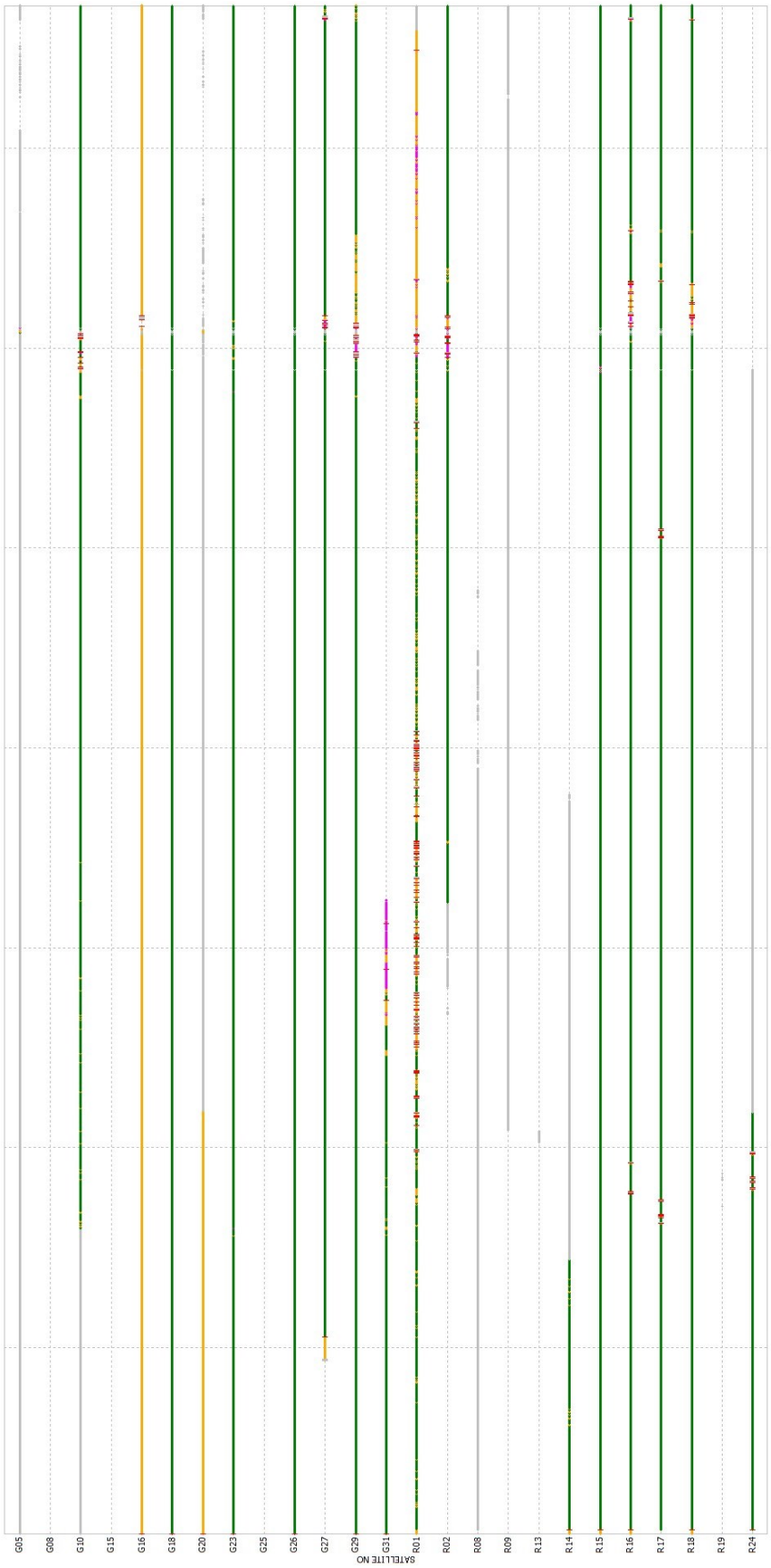

Figure S7. Number of satellites visible at the same time during the acquisition with the GNSS.

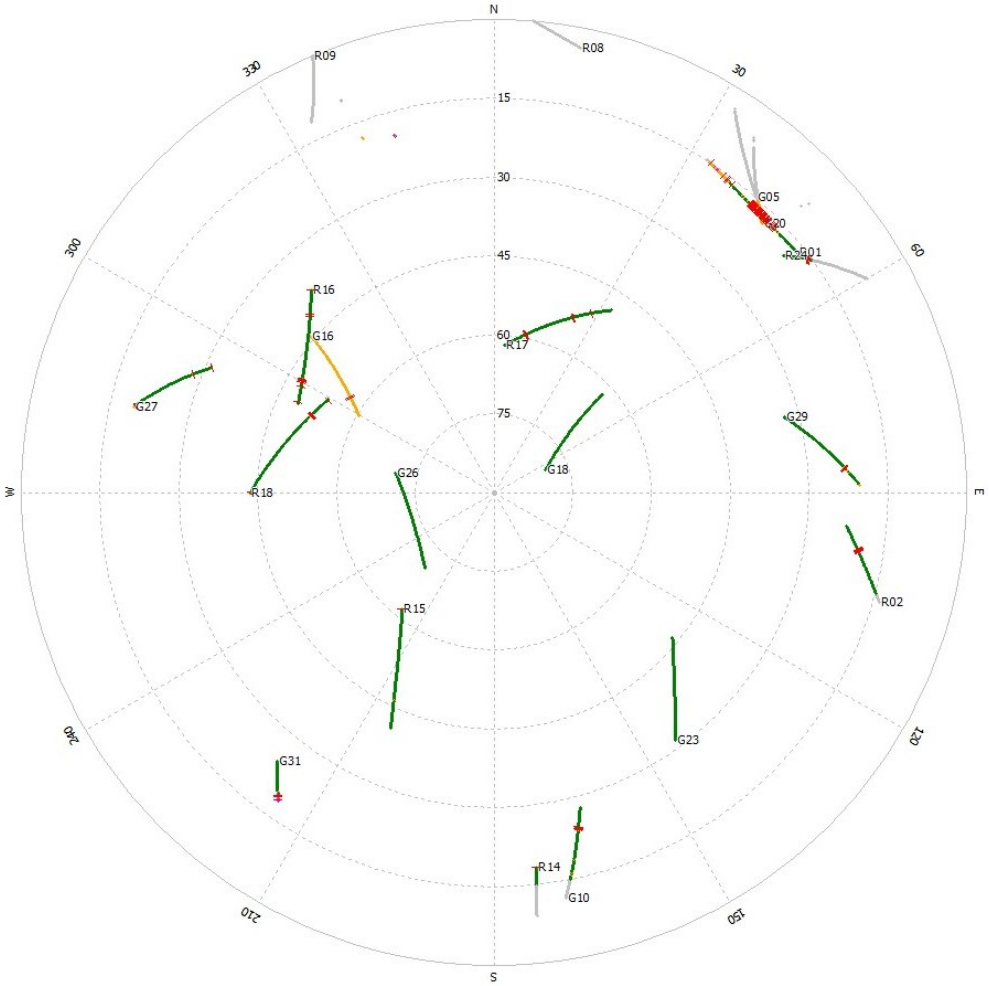

Figure S8. Number of satellites visible at the same time during the acquisition with the GNSS in a skyplot representation.

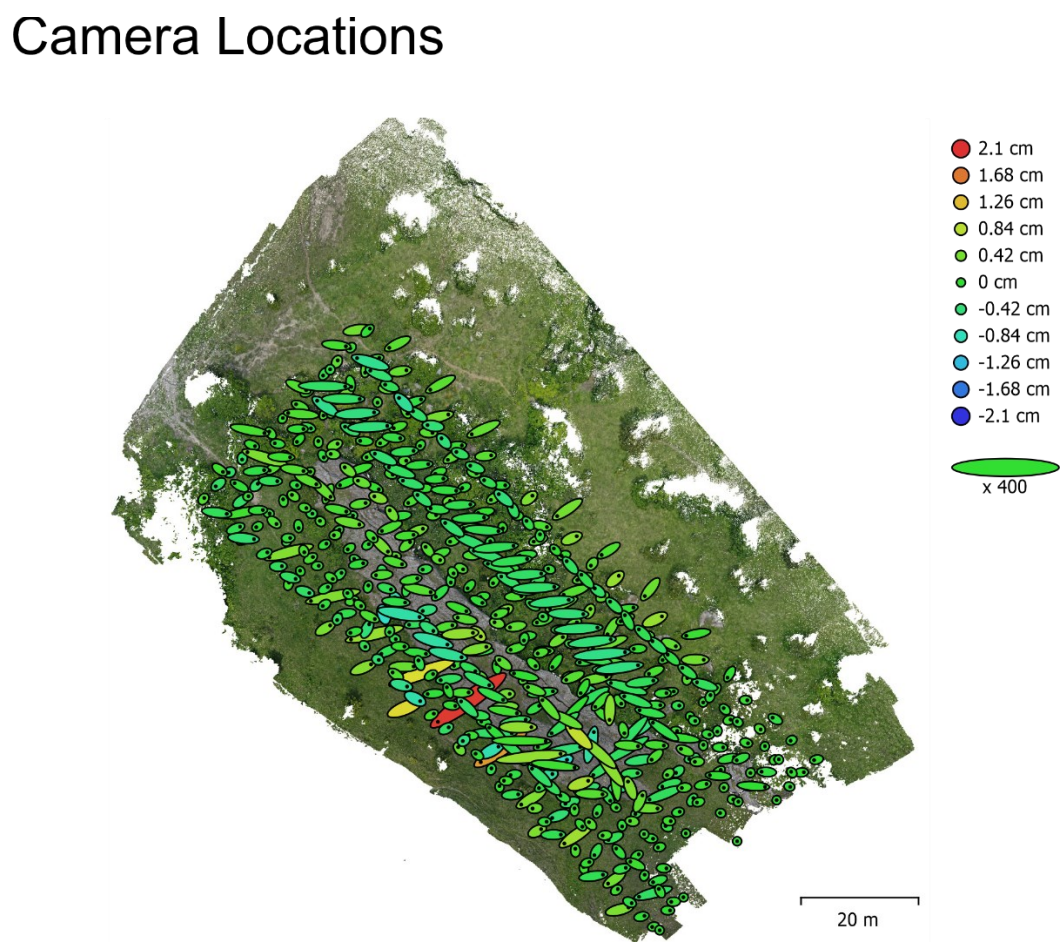

Figure S9. Area A: Camera location and errors estimates. Z error is represented by ellipse color. X, Y error are represented by ellipse shape. Estimated camera location are marked with a black dot.

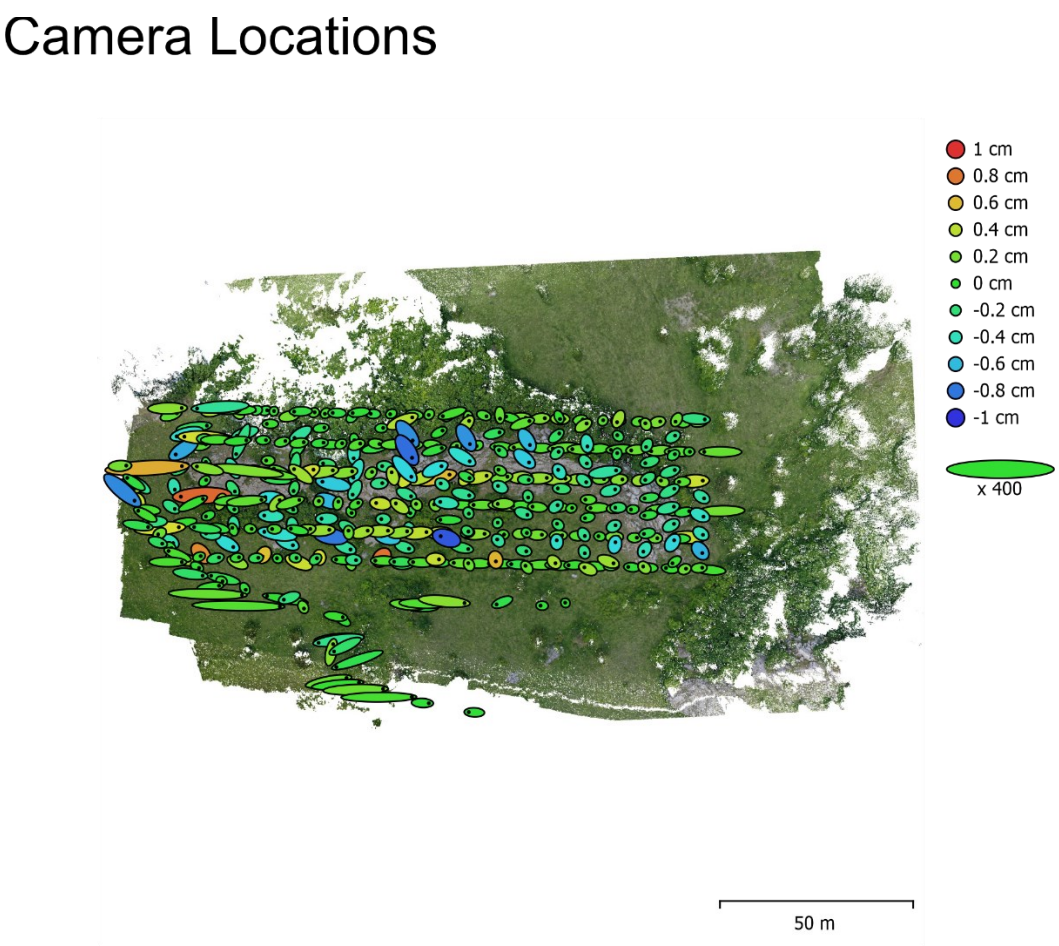

Figure S10. Area B: Camera location and errors estimates. Z error is represented by ellipse color. X, Y error are represented by ellipse shape. Estimated camera location are marked with a black dot.

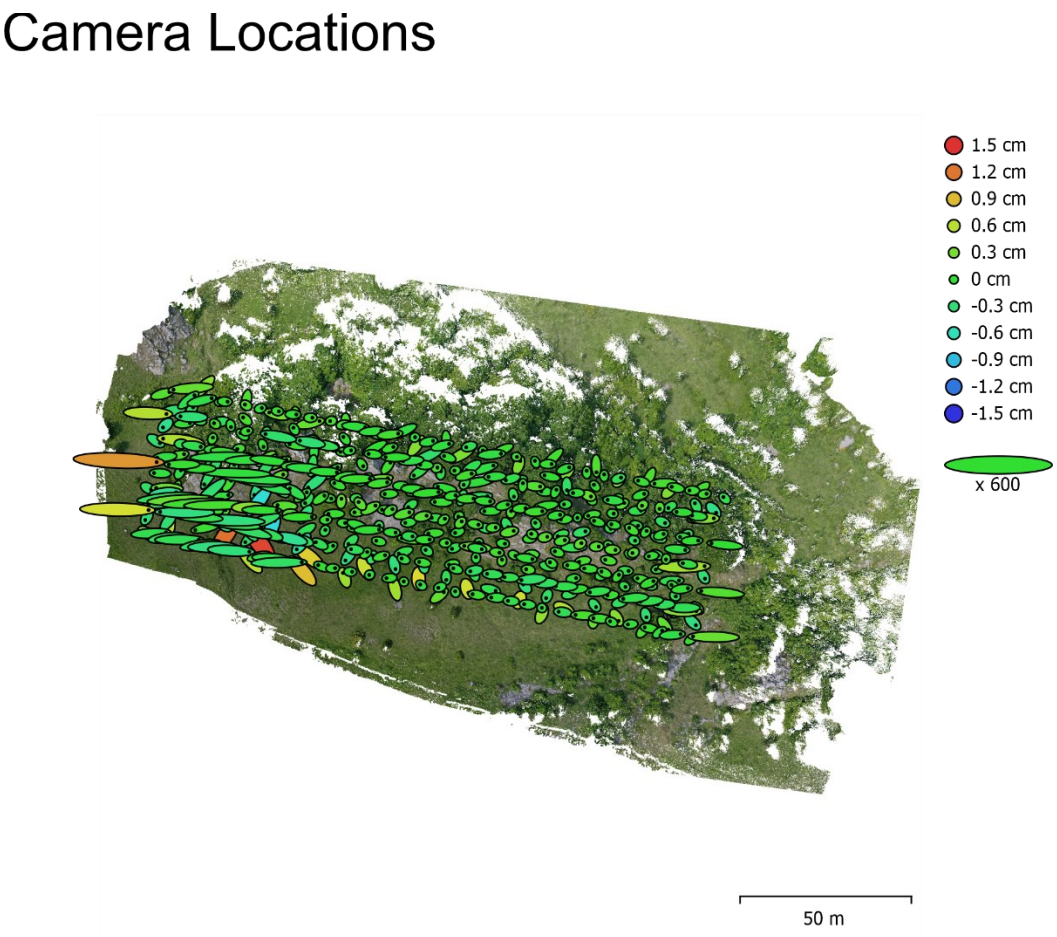

Figure S11. Area C: Camera location and errors estimates. Z error is represented by ellipse color. X, Y error are represented by ellipse shape. Estimated camera location are marked with a black dot.

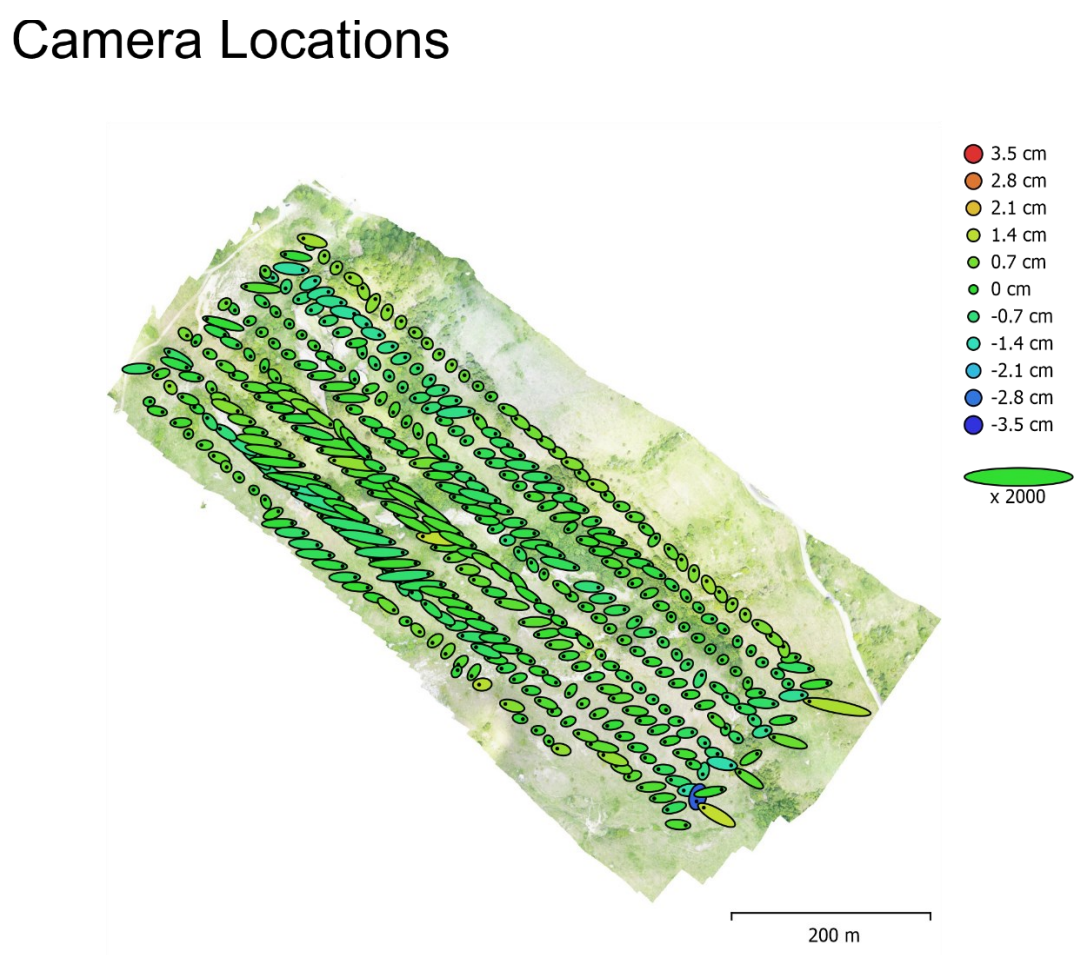

Figure S12. Area Tot: Camera location and errors estimates. Z error is represented by ellipse color. X, Y error are represented by ellipse shape. Estimated camera location are marked with a black dot.

Figure S13. Digital devices used for fieldwork with Fieldmove Clino and Fieldmove apps installed on iPhone and iPad. (**a**), (**b**) and (**c**) show the measurement of a fault plane, a slickenside, and the cleavage, respectively; (**d**), (**e**), and (**f**) Screenshots comparing the Fieldmove app default image and the orthomosaic obtained from the processing in Agisoft Metashape Pro software and subsequent Move suite software; (**g**) and (**h**) show the measurement of the attitude of a normal fault plane; (**i**) slickenside measured using iPad; (**j**) and (**k**) Strike-slip fault and slickenlines measurement. (**l**) bedding attitude measurement.

Table S1. Comparison of the results obtained with Method 1 and Method 2.

Sector	Type	Number of data Method 1	Dip azimuth/Dip mean resultant Method 1	Number of data Method 2	Dip azimuth/Dip mean resultant Method 2	Δ number of data M1-M2	Δ dispersion data Dip azimuth/Dip
1	Bedding	26	321/20	16	320/17	+10	001/03
2	Bedding	17	314/15	60	300/11	-43	014/04
3	Bedding	94	263/23	53	270/11	+41	007/12
4	Bedding	39	243/19	64	220/13	-25	023/06
5	Bedding	40	222/18	80	225/22	-40	003/04
3-4	Fault 1	25	224/70	51	235/69	-26	011/01
3-4	Slickenside F1	25	177/70	51	180/69	-26	003/01
6	Fault 2	7	218/69	43	226/76	-36	009/07
6	Slickenside F2	7	215/69	43	240/73	-36	025/04
5	Joint	6	267/70	19	270/83	-13	003/13
3	Cleavege	52	344/81	12	350/82	+40	006/01

Table S2. Pro and cons of using UAVs technologies.

Pro	Cons
Low cost	Risk of equipment malfunction during flight - Battery failure - Fly away
Variable scale of work and area extent	Errors due to magnetic deviations, manmade or natural
Quick data acquisition on non-vegetated sites	Weather dependent: Limited capabilities for imagery acquisition in the presence of bad weather conditions
Quick data processing (within a few days from collection)	Photogrammetry from UAVs imagery is only reliable on bare earth with minimal or absent vegetation
Employment in emergencies such as, earthquakes and landslides	Possible damage to property and injury to people, in case of flight failure
Employment in hazardous areas minimizing danger and health risks	Analysis of high dataset of images needs high-performance computers
High precision if used with GNSS antennas and PPK technologies	Vulnerable to wild animals
High quality of images and results	Difficult to land in rough areas
	No possibility of automatic flight mode in absence of internet connection